

Chapter 1

Classical phase-sensitive ghost imaging

In the previous chapter, we explored the benefits afforded by quantum OCT over classical OCT, finding that both axial resolution improvement and even-order dispersion cancellation originate not from quantum effects but rather the phase-sensitive cross-correlations between the signal and idler photons in quantum OCT. We then devised a classical phase-sensitive light source by using SPDC in the high-flux, entanglement-breaking regime, after which we implemented phase-conjugate OCT, which realizes the both benefits of quantum OCT using entirely classical light sources and detection. However, there are other ways to construct classical phase-sensitive light sources. In this chapter, we impose computer-generated, pseudorandom phase patterns on two light beams using a pair of spatial light modulators and use it to implement phase-sensitive ghost imaging, another example of an imaging technique previously thought to be exclusive to quantum light sources.

1.1 Background

Ghost imaging is a transverse imaging modality that has been receiving considerable and increasing attention of late owing to its novel physical characteristics and its potential ap-

plications to remote sensing. Ghost imaging exploits the cross correlation between the photocurrents obtained from illumination of two spatially-separated photodetectors by a pair of highly-correlated, partially-coherent optical beams. One beam, referred hereinafter as the signal beam, interrogates a target (or sample) and then illuminates a single-pixel (bucket) detector that provides no spatial resolution. The other beam, which we refer to as the reference beam, does not interact with the target, but it impinges on a scanning pinhole detector or a high-resolution camera, hence affording a multi-pixel output. The term “ghost imaging” refers to the fact that neither photocurrent alone yields a target image, and that the object lies in an arm with no spatially-resolving detectors, but cross-correlating the two photocurrents does produce an image of the object.

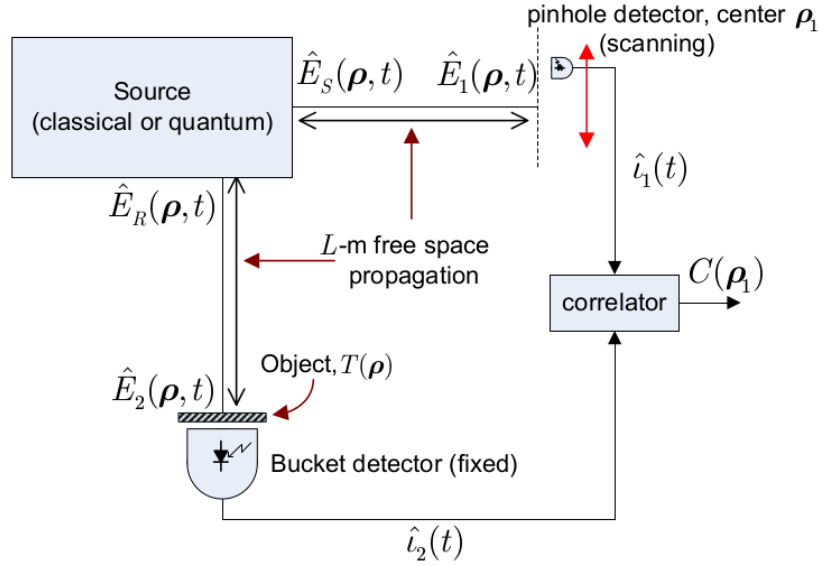


Figure 1-1: Basic ghost imaging schematic.

A basic schematic of the concept of ghost imaging is shown in figure 1-1. Pittman et al. realized the first such ghost imaging experiment [10], in which an entangled signal and idler photons were separated, with an bucket detector on one arm and a spatially-resolving detector on the other arm, and showing that it was possible to image an object placed in the arm with no spatial resolution by counting the coincidences between the two detectors. Al-

though this mode of imaging was inspired by quantum entanglement, subsequent experiments showed that it was possible to achieve a similar imaging result using high-flux, pseudothermal classical light, a rotating ground-glass diffuser followed by a 50-50 beamsplitter, and observing the correlations in fluctuations between the two detectors.

Erkmen and Shapiro later developed a unified theory of ghost imaging with Gaussian-state light [5] that encompasses both biphoton and pseudothermal light sources. In the case of SPDC, a nonclassical phase-sensitive cross correlation between the signal and idler photons is exploited to achieve the ghost image; in the case of pseudothermal light sources, it is a phase-insensitive cross correlation between the two arms as imposed by the ground glass diffuser. However, they also showed the possibility of using unconventional, classical phase-sensitive light sources to achieve ghost imaging. In this chapter, we implement such a system by using spatial light modulators (SLMs) to impose phase-sensitive correlations between two arms.

1.2 Near- and far-field ghost imaging

Erkmen and Shapiro extensively analyzed ghost imaging for the case of jointly-Gaussian signal and reference fields and explored both the near field, where diffraction effects are negligible, and far-field propagation where diffraction spread is dominant. For phase-insensitive coherence propagation, in which the phase patterns of the signal and reference fields are directly correlated (such as the signal and reference arms generated by a rotating ground glass followed by a beamsplitter), the difference between near-field and far-field regimes is defined by a single Fresnel number,

$$D_0 = \frac{k_0 \rho_0 a_0}{2L} \quad (1.1)$$

where k_0 is the k -vector magnitude, a_0 is the coherence radius at the source, ρ_0 is the, and L is the propagation distance to the target, where $D_0 < 1$ indicates being in the far field and $D_0 > 1$ indicates being in the near field [5].

However, for phase-sensitive propagation, in which the phases of the signal and reference beams are anticorrelated at the source plane, the near and far field regimes are defined by two Fresnel numbers: the Fresnel number for diffraction of the coherence length,

$$D_N = k_0 \rho_0^2 / (2L) \quad (1.2)$$

and the Fresnel number for diffraction of the intensity radius,

$$D_F = k_0 a_0^2 / (2L) \quad (1.3)$$

For SLM-based ghost imaging, we assume low coherence where $\rho_0 < a_0$. In this case for phase-sensitive imaging the near-field regime is defined by $D_N > 1$ and the far-field is defined by $D_F < 1$, which is more stringent than the condition for phase-insensitive light [5].

Erkmen and Shapiro showed that in particular, for a transmission mask $T(\rho)$ used as an object, the phase-insensitive far-field ghost image signature is proportional to $|T(\rho)|^2$, whereas the phase-sensitive far-field ghost image signature is proportional to $|T(-\rho)|$ [5]. Thus, for phase-insensitive light we obtain an upright ghost image whereas in the phase-sensitive case we obtain an inverted ghost image. The inverted far-field ghost image is also characteristic of ghost imaging with biphoton sources which also produce only phase-sensitive cross correlations.

1.3 Ghost imaging with spatial light modulators

Similar to our work in PC-OCT described in the previous chapter, we now turn to the implementation of a classical source of signal and reference beams with phase-sensitive cross-correlations that is suitable for ghost imaging. We achieve this by splitting an ordinary continuous-wave laser beam using a 50/50 beamsplitter and imposing computer-generated pseudorandom phase patterns using a pair of synchronized spatial light modulators. By imposing identical phase patterns on the two SLMs we obtain phase-insensitive

cross-correlations; by using opposite phase patterns on the two SLMs we obtain phase-sensitive cross-correlations between the two beams.

1.3.1 Principle of operation

There are two main principles of operation that are used in phase-modulating SLMs today: deformable mirrors, which selectively deform spatial regions over an optical wavelength, and liquid crystal arrays, which exploit electric field-dependent birefringence to impose a phase pattern. SLMs based on deformable mirrors (such as those sold by Boston Micromachines) are insensitive to the polarization of the input beam, may operate at very high modulation frequencies (often in the range of tens of kHz), but may suffer from much higher cross-talk between adjacent pixels since they are mechanically linked. On the other hand, those that are liquid-crystal based (such as those sold by Boston Nonlinear Optics and Hamamatsu) suffer less cross-talk, but only modulate a single polarization axis and are limited to much slower speeds, typically no higher than 50-200 Hz. In this work, we use a liquid crystal-based Boulder Nonlinear Systems Model P512 SLMs which have 512×512 pixels with individually addressable phases. The array size is 7.68×7.68 mm with a pixel fill factor of 83.4%.

1.3.2 Pitfalls

Tests on the P512 SLMs revealed a number of nonidealities. First, although specified to have a maximum switching frequency of 10-30 Hz, we found that this is highly dependent on the phase stroke: while a smooth ramp from a phase of 0 to 2π is accomplishable at upwards of 30 Hz, a sudden step transition from 0 to π , for example, may require ~ 0.3 seconds to settle. Thus, for the purpose of ghost imaging in which we impose uniformly-distributed random phases, we choose to limit the frame rate to about 2 Hz. The limits of the SLM may in fact be better characterized by an analog bandwidth rather than a maximum switching frequency.

Second, the fill factor of the P512 SLMs is 83.4%, with the behavior of the "dead" regions unspecified. Using a lens to image the SLM surface itself onto a camera, half waveplate, and

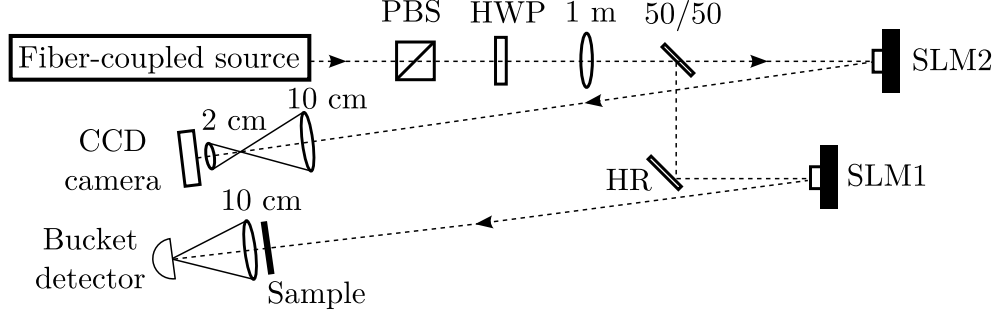


Figure 1-2: Pseudothermal SLM-based ghost imaging setup which can be operated in either phase-sensitive mode (anti-correlated SLM phase patterns) or phase-insensitive mode (identical SLM phase patterns).

polarizer for phase analysis, we found that the dead regions had high cross-talk with the adjacent pixels, which may originate from the electric field imposed by the active area of the pixel.

Third, although the voltage-to-phase calibration provided by Boulder Nonlinear Systems was reasonably accurate for the center region of the SLM, we found that the full SLM surfaces deviated from being flat by as much as a few wavelengths. Xun and Cohn also documented similar distortions in a Boulder Nonlinear Systems SLM [12]. Although in principle a per-pixel calibration could be done, we mitigate this issue by using only the center 128×128 pixels of the SLM where the calibration is reasonably consistent.

1.4 Experimental setup

Figure 1-2 shows our experimental setup. A 10-mW, $\lambda_0 = 795 \text{ nm}$, laser beam was divided by a 50-50 beam splitter into signal and reference, each of which was focused to form a $w_0 \approx 200 \mu\text{m}$ beam waist at its respective liquid-crystal SLM. The polarizing beam splitter and half-wave plate ensured that the SLMs' illumination was vertically polarized. The SLMs (Boulder Nonlinear Systems) have 512×512 pixels (each $15 \times 15 \mu\text{m}$) with individually addressable phases. A control computer generated a 128×128 array of uniformly-distributed random phases (on $[0, 2\pi]$) that were applied to the central 128×128 pixels of SLM1 to

modulate the signal beam with a $\rho_0 = 7.5\,\mu\text{m}$ coherence radius that is much smaller than w_0 . We programmed SLM2 synchronously with the same phase pattern as SLM1 for phase-insensitive cross-correlations, or with its complement for phase-sensitive light. We estimate a phase accuracy of ~ 20 mrad for most cases, with a few small intervals (close to the zero phase end) where we were only able to successfully calibrate to within 50-100 mrad of precision. We generated and updated the SLMs' phase patterns at 2 Hz.

Theory [5] shows that phase-sensitive and phase-insensitive correlations propagate differently, but $D_F \equiv \pi w_0^2/\lambda_0 L \ll 1$, with L being the propagation distance, is sufficient for both to be in their far fields. We used $L = 80$ cm from SLM1 to the object, so that $D_F \approx 0.2$, hence allowing a comparison of far-field phase-sensitive and phase-insensitive ghost images. A 10-cm focal length, 5-cm diameter lens in the signal arm focused the light transmitted through the object on a standard photodetector. An identical 10-cm lens, placed in the reference arm $L = 80$ cm from SLM2, served as the objective for a telescope with a 2-cm focal length eyepiece. This telescope was adjusted to produce a $\sim 5.7\times$ minified image of the speckle pattern on the objective plane. The camera was a shutterless Basler Pilot charge-coupled device (CCD) with 1600×1200 pixels, each $7.4\times 7.4\,\mu\text{m}$ in size with 12-bit dynamic range. We adjusted the CCD exposure and gain parameters to minimize the occurrence of vertical blooming [9], which would degrade the image quality. Figure 1-3(a) displays a typical single-shot CCD image of the far-field speckle pattern in the reference arm produced by one of the random phase patterns at SLM2. The observed ~ 1 mm speckle radius at the objective lens is consistent with the expected far-field coherence radius, $\rho_L = \lambda_0 L/\pi w_0$. The expected spatial extent of the speckle pattern, set by the $2\lambda_0 L/\pi \rho_0 \approx 57$ mm intensity diameter, is slightly larger than the 50-mm lens mount's circular aperture that is visible in Fig. 1-3(b).

The bright central spot in the figure 1-3(a) speckle pattern is an artifact that prevented ghost-image formation in that region. We have traced the artifact to three potential problems in our experimental setup. First, the SLM phase patterns must be uniformly distributed over $[0, 2\pi]$. Second, the polarization of the incident beam must exactly match the active axis of the SLM. Any phase bias or polarization misalignment gives rise to a brighter center

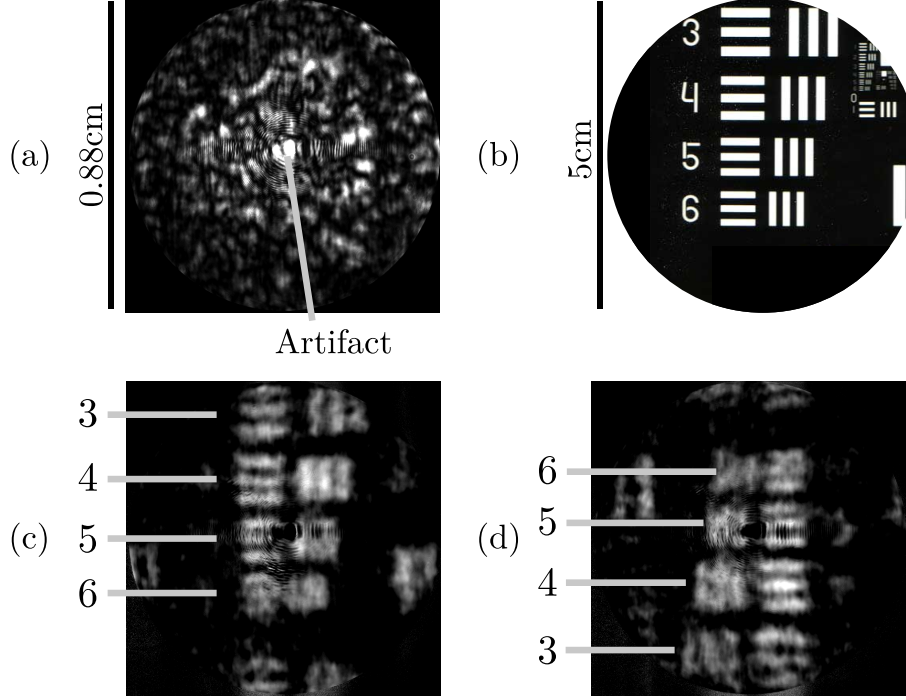


Figure 1-3: (a) Sample single-frame speckle pattern as imaged by the CCD. The artifact in (a) is due to the SLMs' $\sim 83\%$ pixel fill factor. (b) Portion of a USAF spatial-resolution transmission mask used as the object. (c) Phase-insensitive and (d) phase-sensitive far-field ghost images, each averaged over 18640 realizations.

spot, but we were able to resolve these problems by careful SLM calibration and polarization alignment, respectively. The third effect that we observed experimentally as well as confirmed by computer simulation, is that our SLMs are limited by a sub-optimal, $\sim 83\%$ pixel fill factor. The inter-pixel dead space behaves much like a 2-D diffraction grating, creating a grid of spots in the far field including a prominent zero-order spot at the center.

We used elements 3, 4, 5, and 6 from group 2 of a 1951 U.S. Air Force (USAF) resolution transmission test mask for our object, as shown in Fig. 1-3(b), and placed it just before the 10-cm lens in the signal arm. The bucket detector and CCD outputs were fed in real-time to the control computer, which averaged the outputs from a sequence of SLM phase patterns to compute the covariance between each CCD pixel and the bucket detector. That covariance calculation suppressed the background that is otherwise present in classical-state ghost images [5, 7], yielding a high-contrast ghost image of the object.

1.5 Results

Figures 1-3(c) and (d) show the measured phase-insensitive (in-phase SLMs) and phase-sensitive (anti-phase SLMs) ghost images of the test object, each obtained by averaging over 18640 random phase-pattern realizations. The only change made to the setup in transitioning from phase-insensitive to phase-sensitive ghost imaging was to switch the SLM1 and SLM2 patterns from in-phase to anti-phase operation. The image inversion in the phase-sensitive case is in accord with theory [5, 7] for phase-sensitive classical or quantum light sources. Figure 1-4 shows another example of image inversion between far-field phase-insensitive and phase-sensitive ghost imaging—here for an MIT-logo object—obtained using 7000 random phase-pattern realizations.

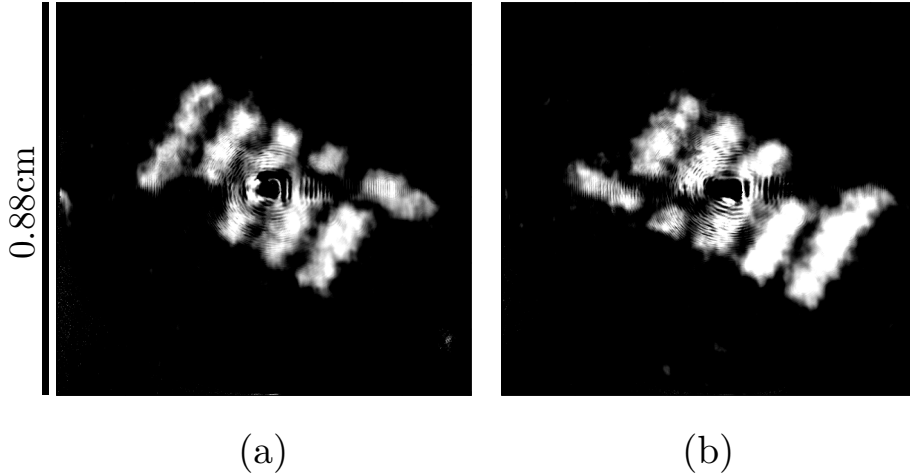


Figure 1-4: MIT-logo ghost images after 7000 realizations for (a) phase-insensitive and (b) phase-sensitive light, showing image inversion in (b). The images are individually normalized, with the noise levels clipped for improved visibility. The bright-spot artifact at the center prevents us from obtaining an image in that small region.

Figures 1-3(c) and (d) show comparable spatial resolutions for the phase-insensitive and phase-sensitive ghost images. The known spacings for the markings on the USAF test mask allow us to evaluate that resolution. In particular, the line spacings for elements 3 and 4 (the largest two elements) are well separated, but those for elements 5 and 6 are less discernible. We thus estimate the spatial resolution to be approximately equal to the spacing between lines in element 4, which is 1.42 mm. This value is in good agreement with theory [5], which

shows that the resolution is speckle-size limited to the object-plane spatial coherence radius $\rho_L \approx 1.0$ mm.

The signal-to-noise ratio (SNR) for a single pixel of a ghost image is defined as the squared-mean value of that image pixel (cross-covariance averaged over all realizations per run) averaged over multiple independent runs of the experiment, divided by the variance of the same image pixel over those runs [5]. Since a reliable SNR measurement over many runs would take a very long time with our equipment, we approximate it by evaluating the values over spatially adjacent pixels (with similar brightness) in a single run. We thus obtain an SNR of ~ 7.5 for the phase-insensitive measurement of Fig. 1-3(c), and ~ 7.9 for the phase-sensitive measurement of Fig. 1-3(d). Because we operated in the narrowband, high-brightness regime with a binary mask, the theoretical SNR for both phase-insensitive and phase-sensitive cases is $\sqrt{2\pi}(T_I/T_0)(\rho_L^2/A_T)$ [5], where T_I/T_0 is the ratio of the integration time to the source coherence time, and A_T is the mask's transmissive area. For our experiment, $T_I/T_0 = 18640$, the number of phase-pattern realizations, and $A_T \approx 3.5$ cm², yielding SNR ≈ 133 for both cases. While the measured SNR for the phase-sensitive and phase-insensitive images are similar, as theory predicts, they are far lower than the theoretical SNR. We believe that this reduction could be partially due to inaccuracies in calibration between SLM1 and SLM2 which would degrade the resulting ghost image. In addition, our spatial approximation may have failed due to variations in brightness at different pixels or in the far-field speckle pattern, causing the spatially-averaged SNR to reach an asymptote. We notice in tests that for lower numbers of realizations (under 2000) the spatially-averaged SNR tracks more closely the theoretical value; this issue is under further investigation.

Our experiments show that phase-sensitive ghost images are badly degraded for tightly-focused illumination when the SLMs are not located at the beam waist, whereas loosely-focused illumination makes these ghost images far less sensitive to the axial displacement of the SLM from the beam waist. For phase-insensitive ghost imaging, however, there is very little sensitivity to SLM position relative to the beam waist. These behaviors were demonstrated by using only the spatially-resolving CCD arm to simulate both the signal

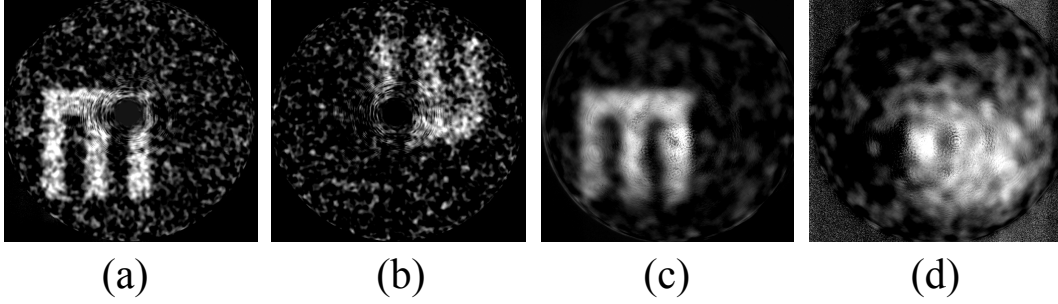


Figure 1-5: Far-field ghost imaging under loose focusing ($w_0 = 150 \mu\text{m}$) for (a) and (b), and tight focusing ($w_0 = 50 \mu\text{m}$) for (c) and (d), with the SLM located at a distance of $2.75\times$ the Rayleigh range z_R . The mask is an off-center letter M. Phase-insensitive images in (a) and (c) are not affected, but phase-sensitive measurements in (b) and (d) show degradation that is severe for tight focusing in (d).

and reference paths as follows. In the first measurement frame we set the SLM to the reference pattern and collected a CCD image of the far-field speckle pattern. In the second frame we set the SLM to the signal pattern, imposed a mask (object) on the camera's image using software, and summed pixel outputs to simulate the bucket detector. This approach avoided potential misalignment between the two physical arms, enabling clean observation of differences between loose versus tight focusing. Figure 1-5 shows our phase-insensitive and phase-sensitive measurements taken under loose ($w_0 = 150 \mu\text{m}$) and tight ($w_0 = 50 \mu\text{m}$) focusing with the SLM located $2.75\times$ the Rayleigh range $z_R = \pi w_0^2 / \lambda_0$ behind the beam waist for each case. The results show that tight focusing and misplacement of the SLM caused significant degradation of the phase-sensitive ghost image. The physical explanation is that the spherical phase-front present on a mislocated SLM due to tight focusing adds the same amount of pixel-dependent phase bias to the signal and reference beams such that their phases are no longer anti-correlated. Because phase-sensitive ghost imaging requires the phases of the signal and reference beams to be anti-correlated, this pixel-dependent phase bias impairs formation of the the phase-sensitive ghost image. Phase-insensitive operation, however, only requires that the two arms have equal phases, so that identical focusing and SLM placement in both arms suffices to produce a high-quality ghost image.

1.6 Signal-to-noise ratio

Erkmen and Shapiro showed that the signal-to-noise ratio (SNR) scales linearly in the number of realizations and is given by [6, 7]:

$$\text{SNR} = \sqrt{2\pi} \frac{T_1}{T_0} \frac{\rho_0^2}{A_T} |T(\rho_1)|^4 \quad (1.4)$$

where $T(\rho)$ is the field transmission mask, T_0 is the coherence time, T_1 is the averaging time, ρ_0 is the coherence radius, and A_T is the total area over which $T(\rho) = 1$. A_T/ρ_0^2 is the number of spatial resolution cells, and for an SLM-based experiment with discrete realizations, T_1/T_0 is the number of realizations. Figure 1-6 shows a sample of an experimental SNR curve for a simple square transmission mask with alongside the theoretical curve, which is in good agreement until the SNR flattens at around 45, which we reach at around $N = 3000$ realizations.

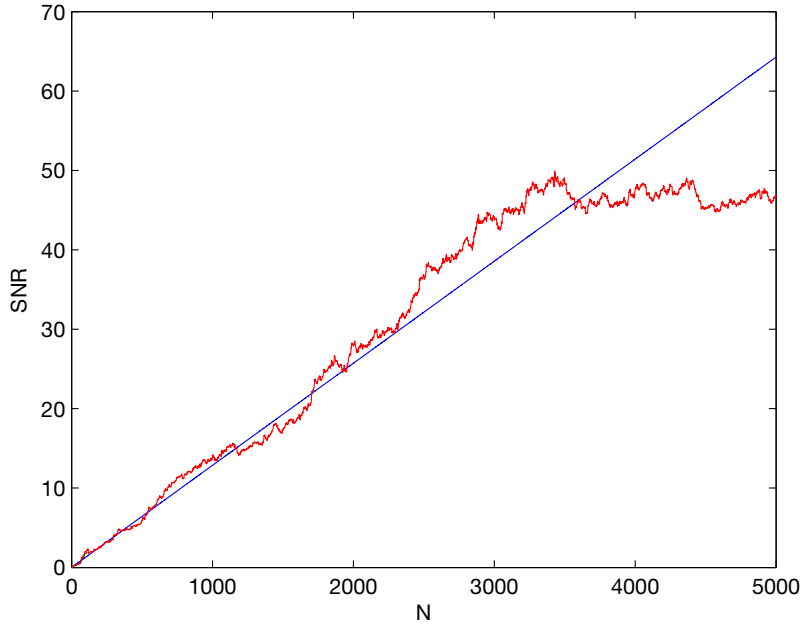


Figure 1-6: Theoretical (blue) and experimental (red) signal-to-noise ratio curves for a simple square transmission mask as a function of the number of realizations N .

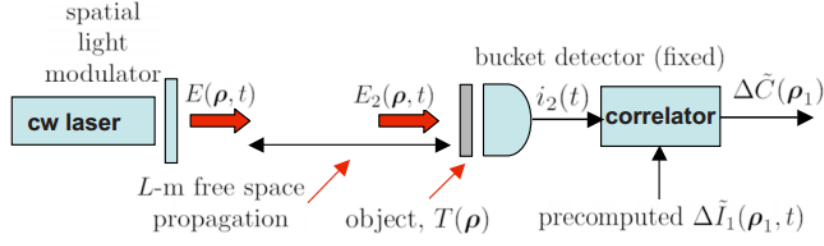


Figure 1-7: Computational ghost imaging schematic, in which there are no spatially resolving detectors and the reference arm is replaced by a computer simulation.

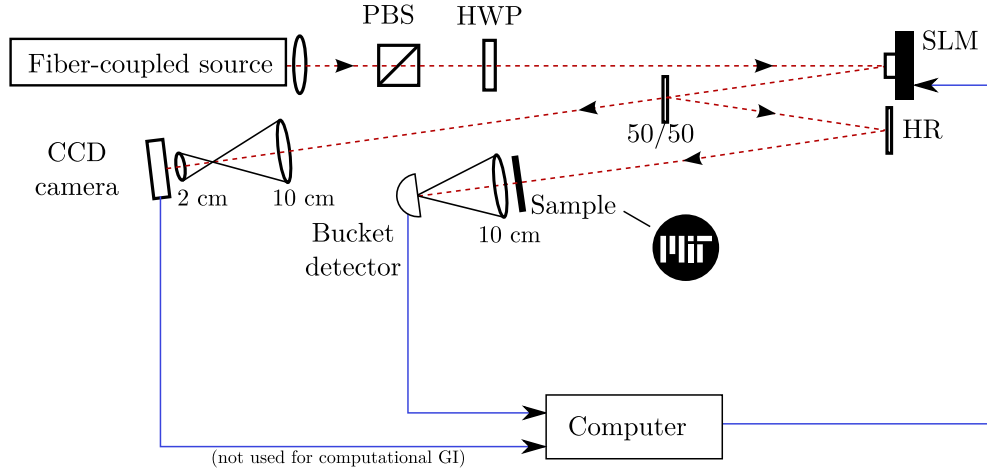


Figure 1-8: Pseudothermal, phase-insensitive ghost imaging setup used to test computational and compressed ghost imaging. In computational ghost imaging, we do not use the CCD camera.

1.7 Computational ghost imaging

In the case of pseudothermal or SPDC-based light sources, the cross-correlations between the signal and idler fields are inherently random. However, SLM-based ghost imaging uses deterministic, pseudorandom modulations imposed by a computer. Since ghost imaging is a product of classical coherence propagation [5], we can in principle eliminate the reference arm altogether and replace it with a computational simulation of its physics, as proposed by Shapiro [11, 7]. As shown in figure 1-7, this permits us to image an object using only a signal arm, without any spatially-resolving detectors.

In order to realize this simulation, we consider the source field $E_R(\rho, t)e^{i\omega_0 t}$ at the SLM plane of the hypothetical reference arm, which is a product of the original cw laser beam field and the phases that would have been deterministically imposed on the reference arm SLM. In the case of phase-insensitive ghost imaging, these would be identical to the phases imposed on the signal arm; in the case of phase-sensitive ghost imaging, they would be the negative. We assume the SLM to be a square of size $D \times D$, with square pixels of size $d \times d$. Since d is much smaller than the beam waist at the SLM, the light field can be approximated over each pixel as a plane wave. The sum of these plane waves at pixels indexed by $n = \{1 \dots (D/d)^2\}$, multiplied by the phases $\phi_n(t)$ deterministically imposed on them, yields an SLM-plane field

$$E_R(\rho, t) = \sum_n \text{rect}\left(\frac{x - x_n}{d}\right) \text{rect}\left(\frac{y - y_n}{d}\right) e^{i\phi_n(t)} \quad (1.5)$$

where $\text{rect}(\cdot)$ is the unit-length rectangle function. We assume quasimonochromatic paraxial diffraction over a free-space path of length L between the SLM and the CCD of the reference arm yields a CCD-plane field E' of [8]:

$$E'_R(\rho', t) = \sum_n \frac{d}{\lambda_0 L} \text{sinc}\left(\frac{x'd}{\lambda_0 L}\right) \text{sinc}\left(\frac{y'd}{\lambda_0 L}\right) e^{-ik_0(x'x_n + y'y_n)/L} e^{-ik_0(|x'|^2 + |y'|^2)/2L} e^{i\phi_n(t)} \quad (1.6)$$

where $\rho_n = (x_n, y_n)$ is the center of pixel n .

The far-field intensity pattern which would have been recorded by the reference arm CCD is then given by $I'(\rho, t) \propto |E'(\rho, t)|$. Figure 1-9 shows a sample pseudorandom phase pattern with IID uniform phase values over $[0, 2\pi]$, and the resulting computed far-field intensity pattern.

We test computational ghost imaging by first switching to a phase-insensitive ghost imaging setup using a single SLM and a beamsplitter, as shown in figure 1-8. This eliminates any differences between the behaviors of two SLM devices. We perform computational ghost imaging in a fashion similar to traditional ghost imaging, using this far-field intensity pattern in place of a CCD image in the reference arm. In figure 1-10 we show side-by-side results of

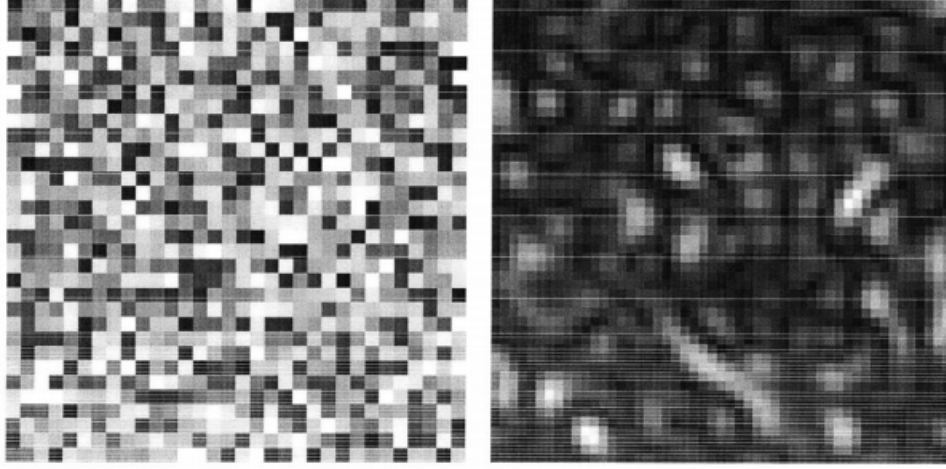


Figure 1-9: (a) Sample pseudorandom phase pattern imposed on SLM. The phase modulation at each pixel is an IID uniform random variable from 0 to 2π and encoded as a greyscale value in this visualization. (b) Simulated result of the far-field speckle pattern.

traditional ghost imaging and computational ghost imaging, realized over 9600 independent pseudorandom phase patterns, noting that the speed of image formation is similar in both cases. Bromberg et al. [1] also performed a similar experiment.

By replacing the reference arm with a computer simulation and using only a single bucket detector in the signal arm to obtain almost identical results, we show that pseudothermal ghost imaging relies on simple classical coherence propagation, and not non-local quantum correlations.

Although not explored significantly in this research, computational ghost imaging also provides a number of advantages over traditional ghost imaging. First, the elimination of the reference arm allows for a simpler device; this is useful for field applications where building a reference arm of the required length would be impractical. Second, computational ghost imaging can be used to image objects at wavelengths where bucket detectors are available but CCD arrays are not. Third, the intensity patterns can be simultaneously computed at multiple depths for a single phase pattern, allowing depth-of-field effects to be exploited to gain some degree of range resolution. These advantages are discussed in detail in [7].

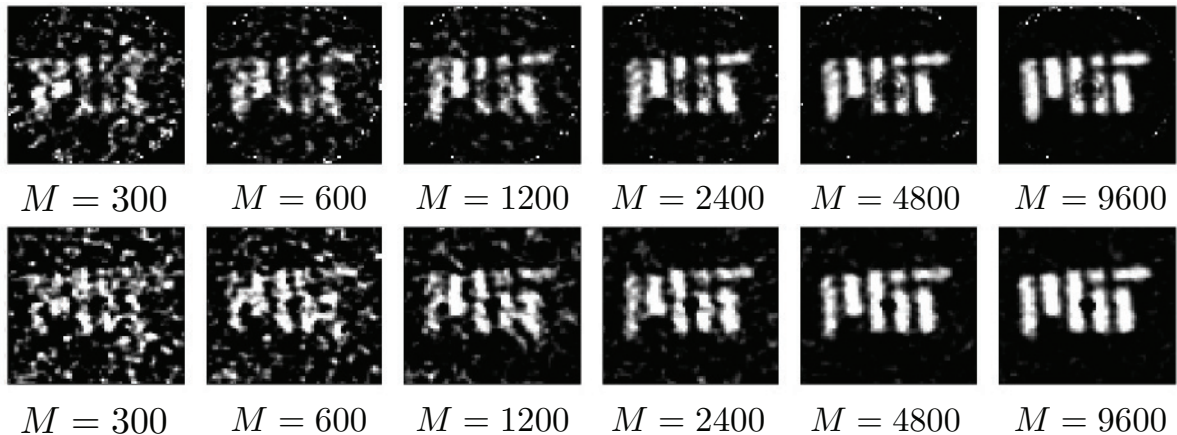


Figure 1-10: Side-by-side results of an MIT logo mask imaged using (a) traditional ghost imaging with optical signal and reference arms and (b) computational ghost imaging in which the reference arm is replaced by a computer simulation, averaged over $M = 300$ to 9600 independent pseudorandom phase patterns.

1.8 Compressed ghost imaging

We now reinstate the experimental reference arm in figure 1-2 and consider another variation of ghost imaging, in which we focus on the processing of our results to significantly reduce the required acquisition time. In this section we make use of compressed sensing (CS) [3], a novel processing technique which has been applied to numerous fields of imaging, notably single-pixel cameras [4], which are very similar in nature to signal arm of a ghost imaging setup.

The basic idea behind compressed sensing is that given that real-world objects exhibit some degree of spatial structure, a small number of measurements of known, random linear projections of the object contains enough information to reconstruct the object. This spatial structure is captured by sparsity in some transform basis, such as the discrete cosine transform (DCT) or wavelet basis. In other words, we expect that most real-world objects have relatively a small number of nonzero coefficients in the transform basis.

Making this very realistic assumption drastically reduces our solution space, and consequently the number of measurements required for faithful reconstruction, a method first proposed by Candes et al. [3]. Rather than using averaging to slowly converge toward

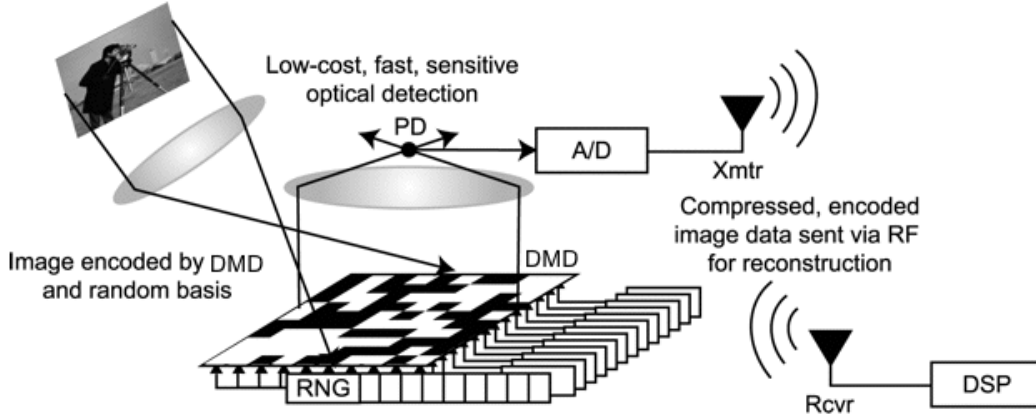


Figure 1-11: Schematic of the Rice University single pixel camera from [1]. DMD: Digital micromirror device, PD: Photodetector, DSP: Digital signal processor, RNG: Random number generator.

our solution over thousands of realizations, we instead use a relatively low number of measurements, treat the image as a solution to an underdetermined linear system, and employ computational optimization techniques to move to a solution that fits our sparsity criteria. Sparsity is usually quantified in terms of the L1 norm of the coefficients in the transform basis [3], which allows us to employ well-known, efficient convex optimization algorithms to quickly search for a global optimum.

Compressed sensing was used by the single-pixel camera at Rice University [4], duplicated here in figure 1-11. The single-pixel camera uses a digital micromirror device (DMD), whose pixels can be set to selectively reflect light, placed at the image plane of a camera, and a single-pixel photodetector to collect all the light reflected by the DMD. Although their implementation placed the DMD at the receiver, allowing it to be used with arbitrary illumination sources, the single-pixel camera could in principle be accomplished by using a custom, broadband light source and spatially modulating the illumination using the DMD (i.e. projecting known illumination patterns onto the object).

This operation of the single-pixel camera is functionally similar to ghost imaging in that a pseudorandom spatial pattern is projected onto the object and the single-pixel detector

is equivalent to a bucket detector. The only difference relevant to data processing is that in ghost imaging, we are unable to arbitrarily configure the intensity pattern at the object plane; we can only configure the phase modulations at the SLM and determine the resulting far-field intensity pattern at the object plane either experimentally (using a reference arm) or by simulation (using computational ghost imaging). However, as long as we have knowledge of these patterns, we can employ the compressed sensing technique that is associated with single-pixel cameras.

To computationally reconstruct a $N \times N$ -pixel image $x_{i \in [0, N^2]}$, we solve for

$$\hat{x} = \arg \min_x ||W\{x\}||_1, \text{ s. t. } Ax = b \quad (1.7)$$

where x is a 1-by- N^2 vector representing the pixels of the image rearranged as a single column, A is a M -by- N^2 matrix containing $M \ll N^2$ realizations of object-plane intensity patterns, one pattern per row and rearranged in the same order as x , b is a M -by-1 vector that stores the resulting bucket detector measurements for each pattern, and $W\{\cdot\}$ is a sparsifying transform (such as DCT, for example). Assuming the system operates perfectly and delivers the correct observations for b , this equation determines the sparsest solution x that satisfies the underdetermined equation system $Ax = b$.

However, since b will be corrupted by noise, in most experimental situations it is necessary to relax this equality constraint. We do this by solving instead for

$$\hat{x} = \arg \min_x ||W\{x\}||_1, \text{ s. t. } ||Ax - b||_2 < \epsilon \quad (1.8)$$

where ϵ represents the maximum magnitude of the error in the bucket detector measurements. This optimization problem can be solved efficiently using convex optimization techniques. We make use of the L1-Magic [2] package for MATLAB which is designed specifically to solve this problem. Another similar method to relax the equality constraint is to solve for

$$\hat{x} = \arg \min_x \left[||W\{x\}||_1 + \frac{1}{2\rho} ||Ax - b||_2^2 \right] \quad (1.9)$$

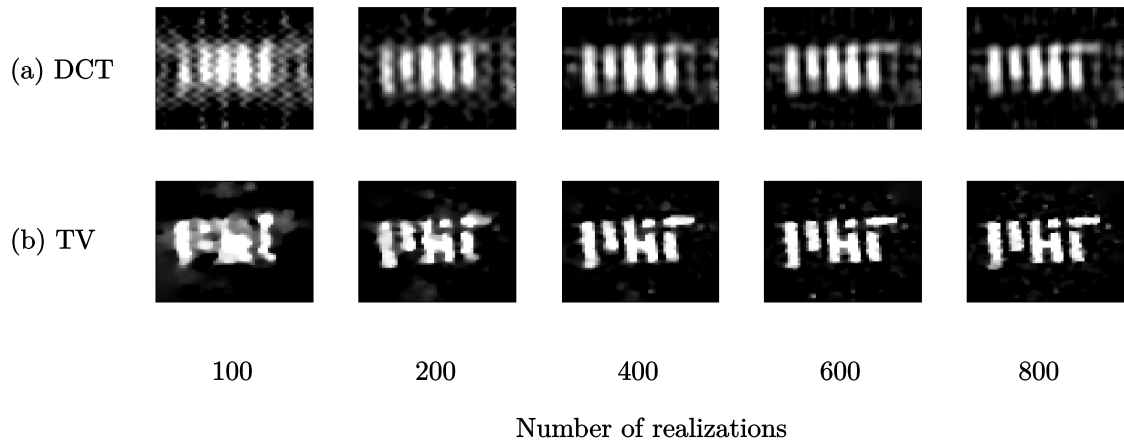


Figure 1-12: Ghost images processed using compressed sensing for a binary MIT logo mask, using (a) DCT and (b) TV sparsifying transforms.

for a tunable relaxation parameter ρ which can be solved using the YALL1 package [13] developed at Rice University.

We also compare compressed sensing to traditional processing based on the second-order cross-correlations between the reference and bucket signals. Figure 1-13 shows side-by-side results of ghost images obtained using traditional averaging and TV compressed sensing using identical data sets. We see in this case that by 200 realizations, the image obtained by compressed sensing is already intelligible, and by 400 realizations it is clear. In contrast, the traditional averaging method is barely intelligible before 1200 realizations; in figure 1-10 of the previous section we observed that it took several thousand realizations to form a high-quality image.

We use the same phase-insensitive ghost imaging setup shown in figure 1-2 and the same mask of the MIT logo. Since this is a binary mask with sharp edges, we note that DCT may not be a suitable sparsifying basis since it is not localized in space and the sharp edges would excite numerous basis components. A more suitable sparsifying transform for this type of

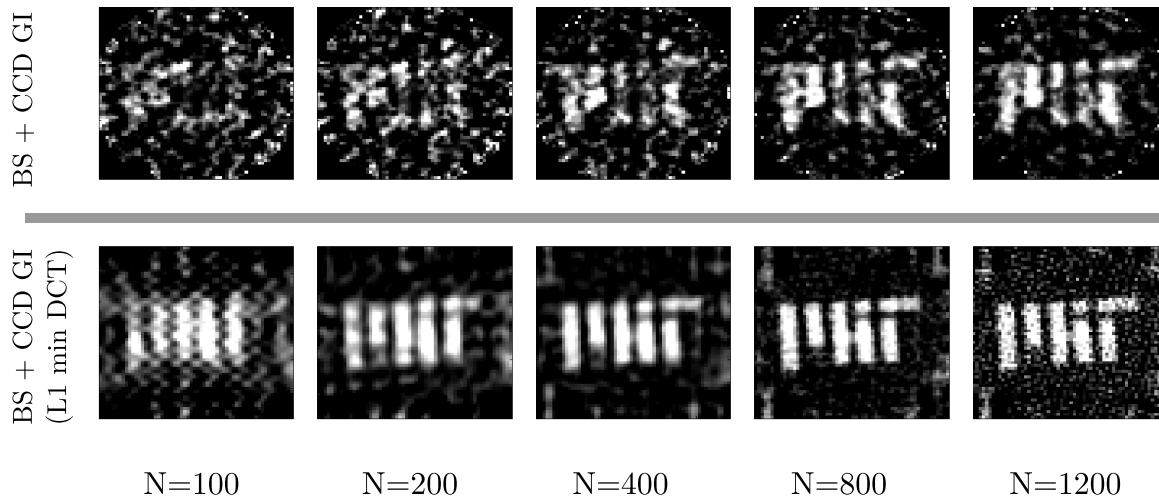


Figure 1-13: Ghost images of an MIT logo mask imaged using (a) traditional averaging and (b) compressed sensing using the same data set.

sample is based on total variation (TV), in which we solve for

$$\hat{x} = \arg \min_x ||\text{TV}(x)||_1, \text{ s.t. } ||Ax - b||_2 < \epsilon \quad (1.10)$$

where $\text{TV}(\cdot)$ represents the sum of the absolute differences of consecutive pixels in the image. This problem is also readily solved by L1-Magic [2]. Figure 1-12 shows results of ghost imaging using compressed sensing using DCT and TV sparsifying transforms, showing that TV does indeed perform better for this particular type of mask. In both cases, we scan over the relaxation parameter ϵ to find an optimal value. as illustrated in 1-14. If the constraint is too tight, artifacts originating from noise remain in the image; if the constraint is too loose, the convex optimization routine over-smoothes the image and arrives at a solution that does not fit the data.

1.9 Computational compressed ghost imaging

We now turn to the question of whether it is possible to entirely replace the reference arm with a computational simulation, and apply compressed sensing techniques at the same time. Figure 1-15 shows sample results of applying our compressed sensing algorithm to the data set used to produce computational ghost images in figure 1-10. We see that although there is bare evidence of an object, we are unable to extract a usable image from this method. We were, however, able to recover images for simpler masks, as seen in figure 1-16.

In order to debug this issue further, in figure 1-17 we reinstate the physical reference arm and compare images obtained by the CCD with our computational simulation; we see a significant discrepancy in the two patterns. We attribute this largely to imperfections in the SLM as described earlier in the Pitfalls section.

1.10 Conclusions

Similar to our work with phase-coherent optical coherence tomography described in the previous chapter, we present phase-sensitive far-field ghost imaging, another example of an experiment previously thought to be exclusive to quantum sources. In addition, we present a new type of classical phase-sensitive light source realized deterministically imposing pseudorandom phase patterns on a pair of light beams using spatial light modulators. We also demonstrate that much like biphoton ghost imaging, phase-sensitive classical ghost imaging also produces an inverted image in the far field.

Finally, we demonstrate a couple of advantages that are unique to classical ghost imaging. First, since we impose deterministic phase patterns, we can eliminate the reference arm from the experiment entirely and replace it with a computer simulation. This also greatly simplifies the setup and allows it to be potentially used for long-range ghost imaging where a physical reference arm would be impractical to implement, or imaging at wavelengths where bucket detectors are available but CCD arrays are not. Such a simulation would not be possible using quantum light sources.

In addition, similar to our PC-OCT experiment described in the previous chapter, our use of classical detectors permits us to operate at much higher power levels and improve acquisition speed. In contrast to quantum ghost imaging experiments which often require hours or more of acquisition time, we were able to obtain clean images within a few minutes with our main limitation being only the SLM frame rate.

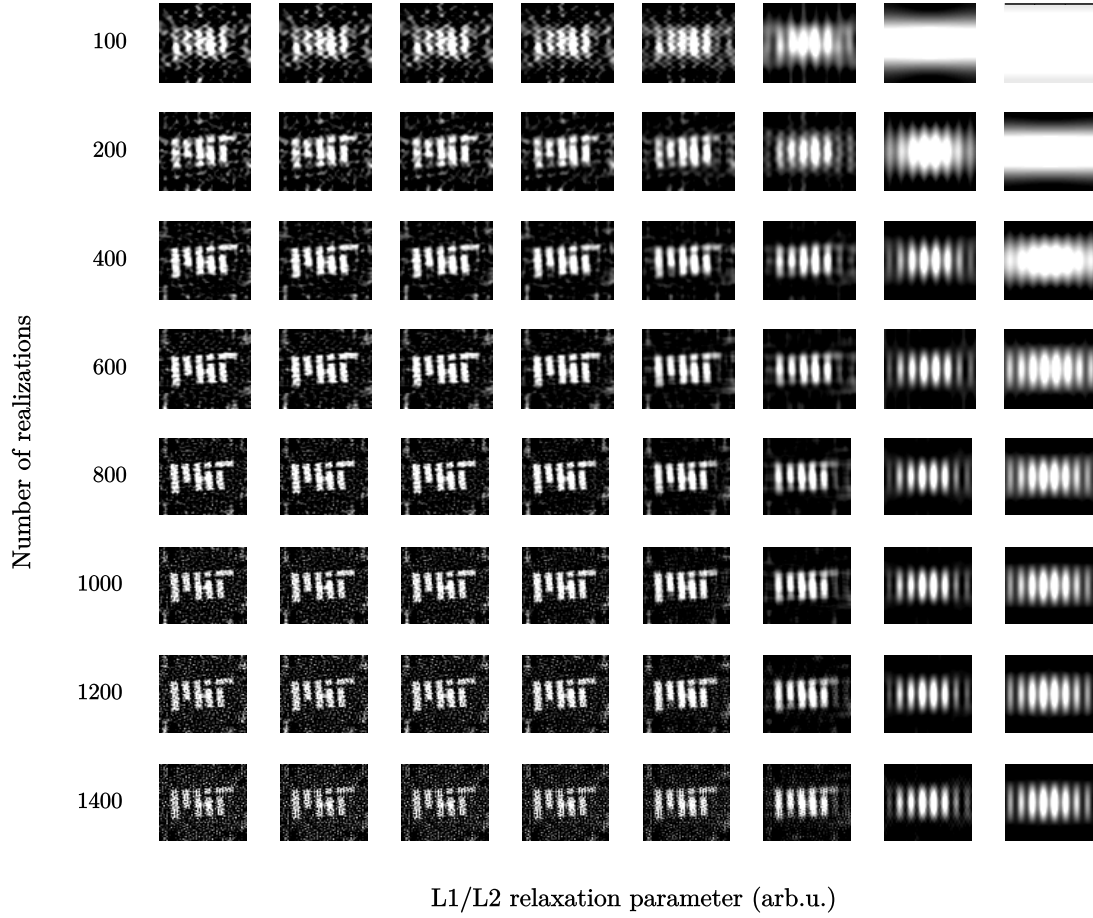


Figure 1-14: Relaxing the constraint to varying degrees in the computational reconstruction using an L1/L2 reconstruction model using DCT as a sparsifying basis. From top to bottom, we increase the number of realizations, and from left to right, we relax the equality constraint, allowing for errors in the data.

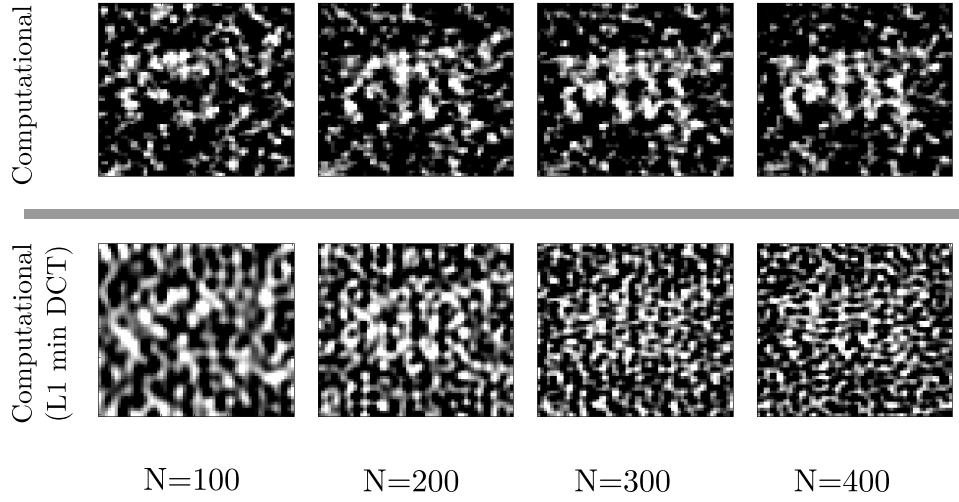


Figure 1-15: Attempts to obtain images of an MIT logo mask imaged using compressed sensing with a computationally-simulated reference arm. (a) shows the computational ghost imaging result using traditional processing, and (b) shows the result of applying compressed sensing techniques.

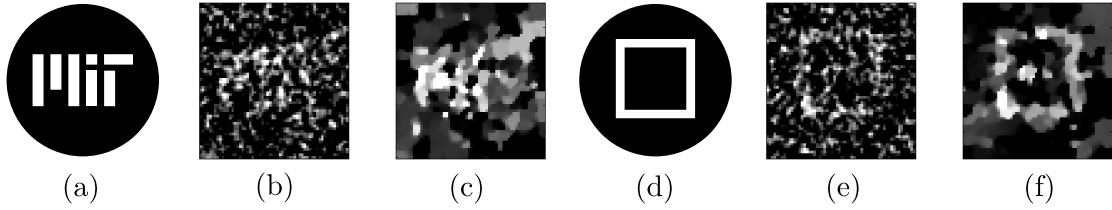


Figure 1-16: Computational compressed ghost imaging using a simpler object. (a) MIT logo mask and ghost image results for (b) covariance-based and (c) compressed sensing using TV minimization for the same number of realizations, showing the same problems seen in figure 1-15. (d) Simpler square mask and results using (e) covariance-based and (f) compressed sensing using TV minimization.

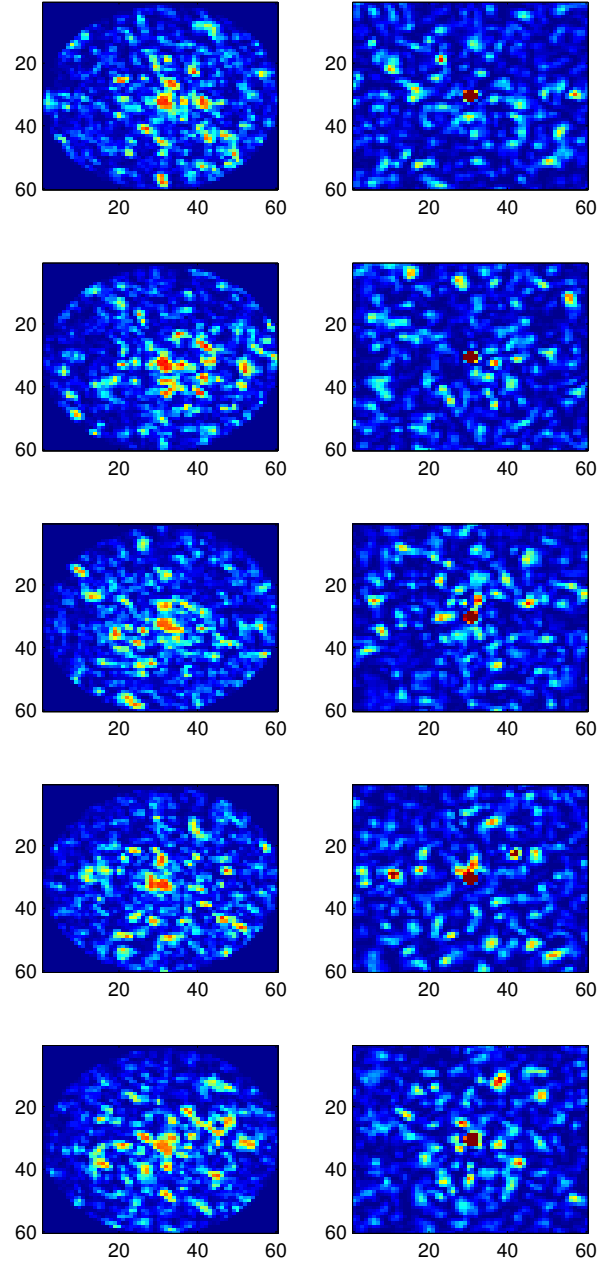


Figure 1-17: Sample speckle patterns acquired by a CCD array (left) and the corresponding computational simulation results (right). We attribute the large discrepancy to imperfections in the SLM array.

Bibliography

- [1] Yaron Bromberg, Ori Katz, and Yaron Silberberg. Ghost imaging with a single detector. *Phys. Rev. A*, 79:053840, May 2009.
- [2] Emmanuel C and Justin Romberg. 1-magic: Recovery of sparse signals via convex programming.
- [3] Emmanuel J. Cands, Justin K. Romberg, and Terence Tao. Stable signal recovery from incomplete and inaccurate measurements. *Communications on Pure and Applied Mathematics*, 59(8):1207–1223, 2006.
- [4] M.F. Duarte, M.A. Davenport, D. Takhar, J.N. Laska, Ting Sun, K.F. Kelly, and R.G. Baraniuk. Single-pixel imaging via compressive sampling. *Signal Processing Magazine, IEEE*, 25(2):83–91, March 2008.
- [5] Baris I. Erkmen and Jeffrey H. Shapiro. Unified theory of ghost imaging with gaussian-state light. *Phys. Rev. A*, 77:043809, Apr 2008.
- [6] Baris I. Erkmen and Jeffrey H. Shapiro. Signal-to-noise ratio of gaussian-state ghost imaging. *Phys. Rev. A*, 79:023833, Feb 2009.
- [7] Baris I. Erkmen and Jeffrey H. Shapiro. Ghost imaging: from quantum to classical to computational. *Adv. Opt. Photon.*, 2(4):405–450, Dec 2010.
- [8] Nicholas D. Hardy. *Analyzing and Improving Image Quality in Reflective Ghost Imaging*. PhD thesis, Massachusetts Institute of Technology, February 2011.

- [9] J. Janesick and T. Elliott. Astronomical ccd observing and reduction techniques. *Astronomical Society of the Pacific Conference Series*, 23:1–67, 1992.
- [10] T. B. Pittman, Y. H. Shih, D. V. Strekalov, and A. V. Sergienko. Optical imaging by means of two-photon quantum entanglement. *Phys. Rev. A*, 52:R3429–R3432, Nov 1995.
- [11] Jeffrey H. Shapiro. Computational ghost imaging. *Phys. Rev. A*, 78:061802, Dec 2008.
- [12] Xiaodong Xun and Robert W. Cohn. Phase calibration of spatially nonuniform spatial light modulators. *Appl. Opt.*, 43(35):6400–6406, Dec 2004.
- [13] J. Yang and Y. Zhang. Alternating direction algorithms for l1-problems in compressive sensing.